# Large-Eddy Simulations of Flow and Heat Transfer in Complex Three-Dimensional Multilouvered Fins

D. K. Tafti, X. Zhang, W. Huang and G. Wang

ACRC TR-165 April 2000

*For additional information:*

Air Conditioning and Refrigeration Center
University of Illinois
Mechanical & Industrial Engineering Dept.
1206 West Green Street
Urbana, IL 61801

(217) 333-3115

*Prepared as part of ACRC Project 94*
*Computational Study Of Multilouvered Fin Heat Exchangers*
*D. K. Tafti, Principal Investigator*

*The Air Conditioning and Refrigeration Center was founded in 1988 with a grant from the estate of Richard W. Kritzer, the founder of Peerless of America Inc. A State of Illinois Technology Challenge Grant helped build the laboratory facilities. The ACRC receives continuing support from the Richard W. Kritzer Endowment and the National Science Foundation. The following organizations have also become sponsors of the Center.*

Amana Refrigeration, Inc.
Arçelik A. S.
Brazeway, Inc.
Carrier Corporation
Copeland Corporation
DaimlerChrysler Corporation
Delphi Harrison Thermal Systems
Frigidaire Company
General Electric Company
General Motors Corporation
Hill PHOENIX
Honeywell, Inc.
Hussmann Corporation
Hydro Aluminum Adrian, Inc.
Indiana Tube Corporation
Invensys Climate Controls
Lennox International, Inc.
Modine Manufacturing Co.
Parker Hannifin Corporation
Peerless of America, Inc.
The Trane Company
Thermo King Corporation
Visteon Automotive Systems
Whirlpool Corporation
Wolverine Tube, Inc.
York International, Inc.

*For additional information:*

*Air Conditioning & Refrigeration Center*
*Mechanical & Industrial Engineering Dept.*
*University of Illinois*
*1206 West Green Street*
*Urbana IL 61801*

*217 333 3115*

# LARGE-EDDY SIMULATIONS OF FLOW AND HEAT TRANSFER IN COMPLEX THREE-DIMENSIONAL MULTILOUVERED FINS

D. K. Tafti, X. Zhang, W. Huang, G. Wang[1]
Application Technologies Division
National Center for Supercomputing Applications
University of Illinois, Urbana Champaign
Urbana, IL 61801.

## ABSTRACT

The paper describes the computational procedure and results from large-eddy simulations in a complex three-dimensional louver geometry. The three-dimensionality in the louver geometry occurs along the height of the fin, where the angled louver transitions to the flat landing and joins with the tube surface. The transition region is characterized by a swept leading edge and decreasing flow area between louvers. Preliminary results show a high energy compact vortex jet forming in this region. The jet forms in the vicinity of the louver junction with the flat landing and is drawn under the louver in the transition region. Its interaction with the surface of the louver produces vorticity of the opposite sign, which aids in augmenting heat transfer on the louver surface. The top surface of the louver in the transition region experiences large velocities in the vicinity of the surface and exhibits higher heat transfer coefficients than the bottom surface.

## INTRODUCTION

In compact heat exchanger applications, air-side thermal resistance accounts for approximately 80 percent of the total resistance. Consequently, a larger surface area per unit volume, and heat transfer enhancement techniques in the form of interrupted or complex flow passages are mandatory in reducing the resistance to heat transfer. Fins have been primarily used to provide an extended surface area for heat transfer from the primary heat source or sink, which in most instances are flat or round tubes. Further, complex or interrupted flow passages in fin geometries have been used to augment the fin heat transfer coefficient by maintaining a high temperature potential between the fin surface and air. This is achieved by thermal boundary layer restarts, and the inducement of large-scale coherent structures to enhance mixing in the vicinity of fin surfaces.

One form of interrupted flow passage which has found wide spread use in heat exchanger applications is the louvered fin surface. A flat-tube louvered heat exchanger with rectangular channels is shown in Fig. 1. Most of the progress in studying this fin configuration has been made through experiments [Chang and Wang, 1997; Beauvais, 1965; Davenport, 1983; Zhang and Lang, 1989; Webb and Trauger, 1991; Achaichia and Cowell, 1988a; Springer and Thole, 1998; Dejong and Jacobi, 1999] and it is only now that computational tools are beginning to play an important role.

Several computational studies of multilouvered geometries have been reported since the 1980s. Various simplifying assumptions made in earlier studies have prevented the use of computations for complete and reliable predictions of multilouvered fins. These studies assumed louvers of zero thickness and/or fully-developed flow conditions [Achaichia and Cowell, 1988b], and/or Cartesian grids with a staircase louver surface [Baldwin et al., 1987]. The late 80s and early 90s saw considerable progress in the Japanese automotive industry in simulating multilouvered geometries. Suga et al. [1989] and Suga and Aoki [1991] used considerable sophistication in their formulation on overlaid grids for representative multilouvered fins. The overlaid grids allowed the use of orthogonal grids aligned with the louvers. On the other hand, Hiramatsu et al.

[1] Currently at ANSYS Inc., Canonsburg, PA 15317.

[1990] used oblique or body-fitted grids in the calculation domain. Halt et al. [1996] have used FLUENT-UNS with hybrid grids. While all the above studies assumed steady laminar flow, Achaichia et al. [1994] studied the flow pattern in multilouvered fins with the commercial code PHOENICS along with the $k$-$\varepsilon$ turbulence model for high Reynolds numbers. Tafti et al. [1999,2000] have applied time-dependent calculations to study flow transition in two-dimensional multilouvered geometries. They found that instabilities first appeared in the wake of the exit louver. Shortly thereafter, the flow became unstable near the exit louvers, and the instability then spread upstream into the bank.

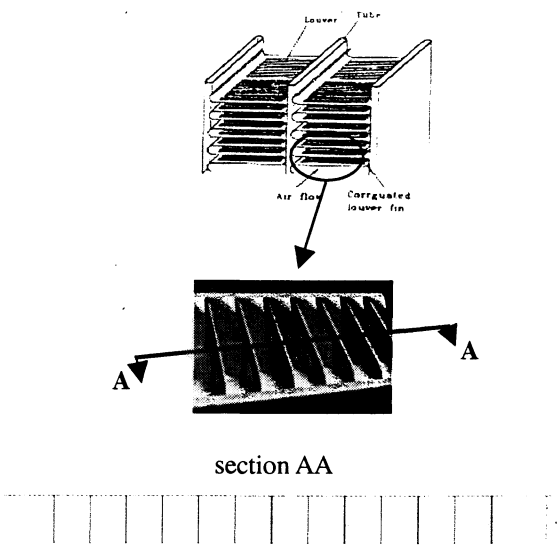


**Fig. 1: Flat tube louvered heat exchanger with rectangular channels. Section A-A shows the two-dimensional cross-section of a fin.**

## Large-Eddy Simulations (LES)

Large-eddy simulation is playing an increasingly important role in the fundamental study of turbulent flows. By resolving only the energy containing eddies, LES reduces the computational complexity of Direct Numerical Simulations (DNS) by several orders of magnitude. However, the application of LES to complex flows still remains elusive for a number of reasons. Chief among them is the high computational and human cost of doing these simulations in complex geometries with complex physics. However, with the exponential increase in computational power in the last decade, the computational barrier is slowly but surely being broken down. The DOE/ASCI initiative, and the recent NSF Terascale initiative will provide multi-Terascale facilities for the US research community in a three-year time frame.

Flows in compact heat exchangers are particularly conducive to the use of LES technology because the operating range of Reynolds numbers encountered is not very high. There are a number of approaches one could use in performing LES. One is to use explicit subgrid scale models. Another is to approach the problem from the point of view of a pseudo-DNS or LES with no subgrid scale model. The third approach is the use of Monotonic Integrated Large-Eddy simulations (MILES). A brief explanation of the three approaches is given here.

### Subgrid Scale Stress Models

There are a number of subgrid scale models varying in complexity from eddy-viscosity to one equation models. Recent reviews can be found in Ferziger [1996] and Lesieur and Metais [1996]. The most widely used closure model, suggested by Smagorinsky [1963], is based on Boussinesq's approximation in which the subgrid-scale Reynolds stresses are related to the strain rate tensor of the resolved field through an eddy viscosity. The eddy viscosity is computed from the resolved strain rate magnitude and a characteristic length scale. The length scale is assumed to be proportional to the filter width *via* a Smagorinsky constant. Germano et al. [1991] proposed a dynamic procedure for the computation of the Smagorinsky constant. The dynamic procedure utilizes information from the resolved high wavenumber scales by applying a test filter in addition to the grid filter to obtain model constants. The original method has been extended to other subgrid scale models [Zang et al., 1993]. The dynamic model has been found to be particularly useful in capturing the near wall behavior of turbulence and in transitional flows [Piomelli et al., 1991], where previously a lot of hand tuning of model constants was necessary. The model has been tested extensively in flow simulations using spectral methods (Germano et al., 1991; Piomelli, 1993; Piomelli and Lui, 1995). Several researchers also have applied the dynamic subgrid scale stress model with finite-difference approximations [Beudan and Moin, 1994; Akselvoll and Moin, 1995; Jordan and Ragab, 1993; Zang et al., 1993]. However, a number of challenges remain in its application to complex turbulent flows. Chief among them are the treatment of inhomogeneous boundaries in devising the test filter [Najjar and Tafti, 1996b] and the localization of the model constant [Ghosal et al., 1995].

Recent work has focused on subgrid stress models based on the similarity model of Bardina et al. [1983]. However, instead of approximating the full field (resolved + subgrid scales) by the resolved field, the subgrid scales are constructed from the filtered field by appropriate defiltering or a deconvolution [Liu et al., 1994; O'Neil and Meneveau, 1997; Domaradzki and Saiki, 1997; Geurts, 1997; Domaradzki and Loh, 1999].

### The MILES Approach

An alternative to the use of explicit subgrid scale models for LES is the use of Monotonic Integrated Large-Eddy simulations (MILES) [Boris et al., 1992]. These encompass a general class of methods which maintain the monotonicity (do not give rise to spurious oscillations) of the integrated field (also referred to as shock capturing schemes, total variation diminishing (TVD), essentially nonoscillatory, positivity preserving, shape preserving). They differ in detail but are designed to support the minimal diffusion that is required to preserve the shape of a distribution during transport. The most widely used monotonicity preserving criterion is the Total

Variational Dimishing (TVD) [Harten, 1984]. The TVD criterion is applied to the cell face values at time level $n$ to generate a monotonic field at time level $n+1$. Leonard [1991] has argued that the TVD limiter is overly restrictive, and the application of monotonicity can be simplified and made much less restrictive if applied directly to the time-averaged face values. The Flux Corrected Transport [FCT] scheme of Boris and Book [1973] is similar in spirit. When used in this context, Leonard's universal limiter or more generally "flux limiting" scheme, allows the use of high-order methods in the calculation of cell face values. Thuburn [1996] has developed a multi-dimensional version of Leonard's universal limiter for strongly deforming meteorological flows.

**LES with No Model**

In finite-volume and finite element discretizations, truncation errors dominate the high wavenumbers of the resolved flow. The use of upwind approximations, dissipate energy in the high wavenumbers. It has been shown convincingly [Najjar and Tafti, 1996a, Mittal and Moin, 1997] that the use of explicit subgrid scale models with these schemes provides additional undesirable net dissipation. Schemes like the second-order central difference scheme on a staggered mesh [Harlow and Welch, 1965], conserve spectral energy but redistribute the energy in the spectrum. The use of this discretization has found favor in LES because in spite of errors, it maintains the integrity of the energy spectrum in the high wavenumbers of the resolved flow, better than dissipative schemes. However, in under resolved flows or flows in which substantial energy is contained in the near grid and subgrid scales, the central-difference schemes are much more prone to instabilities. However, on the flip side, a stable calculation indicates that most of the energy is resolved by the grid. Hence LES with no model follows the philosophy that a stable finite-volume numerical scheme does not need additional dissipation via a subgrid scale model to increase its prediction accuracy.

## Parallel Architectures and Programming Models

Information technology is fast becoming one of the key enabling technologies for making new inroads into science and engineering. High performance parallel computing is an important subset of this field. Here we review some architectural trends and their implications on programming paradigms.

Since their inception in the mid 60s to early 70'-s, parallel computers have been designed in a variety of configurations, differing in the organization of address space, interconnect network, and control mechanism for instructions. In the mid 90's, distributed shared memory (DSM) architectures, which are hybrids between shared and distributed memory architectures, were introduced. The architecture combined shared memory processors at the node level, with distributed nodes interconnected by a network. The early DSM architectures were the HP-Convex Exemplar SPP Series and the SGI-Cray Origin 2000. A variant of the DSM architecture is the idea of interconnecting shared memory processors (SMPs) in a distributed environment. This is now being extended to build supercomputers out of commodity NT or Linux PCs.

Of the top 500 most powerful computers worldwide [Top500, 1999], 69 systems are clusters built with SMPs with more than 16 processors per node, such as the ASCI Blue system at Los Alamos, which contains 48 Origins, each with 128 processors. The ASCI Blue Pacific SST at Lawrence Livermore consists of a 1464 node cluster of 4 way IBM SP604e SMPs and in the acquisition stage is ASCI White, which will consist of 8 SMP processors per node. In addition, in the top 500 list there are 7 clusters built out of commodity parts and SMP nodes with less than 16 processors. It is also envisioned that clusters of DSMs and SMPs will be the architecture of choice for the NSF Terascale Initiative.

Another development on the software side is that application programming paradigms are becoming much less dependent on the architectural aspects, hence increasing portability of codes, assuring a longer life span for software developed. In a clustered DSM/SMP environment, both distributed and shared memory programming models are feasible. Because of the cache-coherent globally shared address space within each SMP or DSM, a shared memory programming paradigm is feasible. An important development in this area is the OpenMP industry standard [KAI, 1997], which replaces vendor specific libraries. However, currently OpenMP has no extensions which can enable this paradigm across a cluster of SMPs or DSMs. Therefore one has to resort to distributed memory programming with explicit communication calls to message passing libraries like MPI [Gropp et al., 1994; MPI2, 1997]. Although a distributed programming model, has a higher cost associated with its use than does shared memory programming on a single DSM or SMP, this paradigm imposes explicit data locality, which can have a significant positive impact on scalability.

Another programming paradigm is to use both, distributed memory programming across a network, and shared memory programming inside each shared memory node or unit. The use of this hybrid paradigm does not limit one to these architectures but rather provides the flexibility of using both or either of these paradigms on other configurations with minimal effort.

In addition to the use of the hybrid MPI-OpenMP across clusters of SMPs or DSMs, one can also use this paradigm within a single DSM unit like the SGI-Cray Origin 2000. Hybrid or embedded parallelism [Tafti and Wang, 1998] has several advantages over either distributed or shared memory parallelism. It can accommodate both coarse grained parallelism at the high level and fine grained parallelism underneath. It maps to the architectural features of a DSM architecture by keeping data locality explicit in the coarse-grained parallelism and allowing the fine grained shared memory parallelism to take advantage of the data locality. Further, embedded parallelism also complements the concept of hierarchical domain decomposition [Smith et al., 1996] for

cache friendly and scalable algorithms [Cai et al., 1996; Anderson et al., 1999; Wang and Tafti, 1998a-b, 1999].

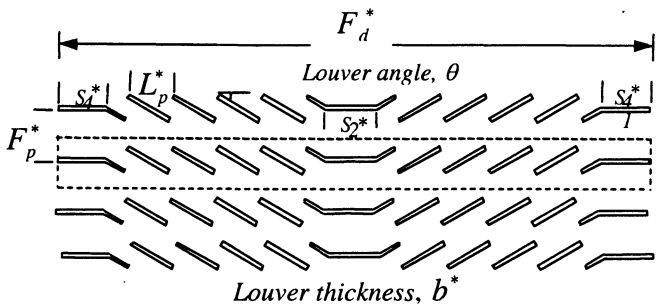


**Fig. 2: Two-dimensional geometrical parameters in multilouvered fins.**

## General Flow and Thermal Characteristics in Multilouvered Fins

Fig. 2 shows a multilouvered fin with its characteristic dimensions. $L_p^*$ is the louver pitch, $F_p^*$ is the fin pitch, $b^*$ is the louver thickness, and $\theta$ is the louver angle[2]. The heat transfer characteristics of the multilouvered geometry is governed by three important effects :

a) Duct directed versus louver directed flow: When the bulk of the flow in the louver bank is aligned with the streamwise direction, it is referred to as duct directed flow. This was first recognized by [Davenport, 1983] and studied by other researchers in the field [Webb and Trauger, 1991]. Fig. 3 illustrates the two cases. Duct directed flow has a detrimental effect on the heat capacity and heat transfer coefficient, since a very small fraction of the fluid flows between louver passages. On the other hand, louver directed flow has a large positive impact on the heat transfer coefficient. High Reynolds numbers, large louver angles, small fin pitches, and large louver pitches are conducive to louver directed flow.

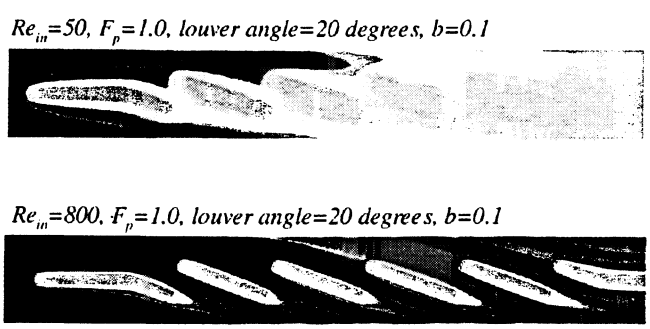


**Fig. 3: Mean thermal fields illustrating (a) duct flow; (b) louver directed flow.**

[2] Dimensional quantities are denoted by the superscript $^*$.

b) Onset of unsteadiness: The onset of unsteadiness augments the heat transfer coefficient [Zhang et. al, 1997a-b]. Fig. 4 compares the heat flux distribution on a louver at two Reynolds number. At the lower Reynolds number the bottom surface of the louver has a large recirculation zone, which becomes unstable at the higher Reynolds number. The instability leads to the periodic shedding of large scale spanwise vortical structures, which enhance mixing near the louver surface [Tafti, 1993]. This is reflected in the sharp jump in the heat flux distribution on the bottom louver surface. Large louver angles, large ratios of fin pitch and fin thickness relative to louver pitch lead to the earlier onset of unsteadiness.

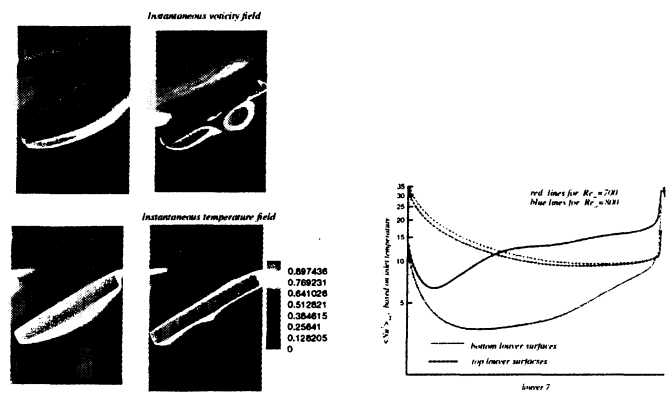


(a) (b)

**Fig. 4: Instantaneous z-vorticity and temperature contours for two Reynolds numbers. With the onset of vortex shedding, the thick thermal boundary boundary is destroyed. This results in a large increase in mean heat flux.**

c) Thermal wake interference: Fig. 5 illustrates the different types of thermal wake interference which can occur. Intra-fin interference occurs between louvers in the same fin, and is strong when the flow is duct directed. The interference of wakes from louvers upstream of the re-direction louver on downstream louvers of the same fin is yet another manifestation of intra-fin interference. This usually is of a secondary nature. Inter-fin interference occurs between adjacent rows of fins when the flow is louver directed. Both intra- and inter- types can have a large effect on the total heat capacity of the fin, whereas the latter does not have a large effect on the heat transfer coefficient.

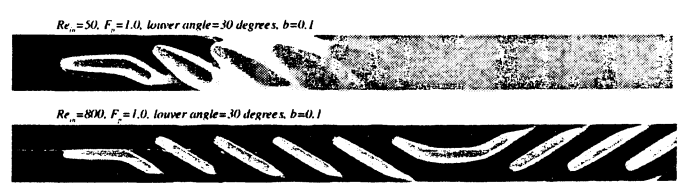


**Fig. 5: Illustration of intra-fin and inter-fin thermal wake interference.**

These three phenomena can be captured with good precision in two-dimensional simulations. Effects (a) and (c) are primarily dependent on the two-dimensional geometrical parameters. The onset of unsteadiness is primarily a two-dimensional phenomenon, which can either be classified as a wake or Kelvin-Helmholtz instability [Tafti, et al., 2000], and can be resolved with accuracy in the initial stages of development. However, there is evidence [Zhang et al., 1997a-c], that as the Reynolds number increases beyond $\mathrm{Re}_{D_h}$ (based on hydraulic diameter) of around 2000-2500, secondary three-dimensional instabilities might be important. The intrinsic three-dimensionality, which develops in the flow field, cannot be resolved with two-dimensional simulations. It has the effect of diffusing the coherence of the vortical structures, which travel along the louver surface and reduce their effectiveness in enhancing heat transfer. For Reynolds numbers, $\mathrm{Re}_{D_h} > 2500$, this effect may be important. However there has not been any systematic evaluation of this effect, partly because the operating range of multilouvered heat exchangers does not exceed far beyond this point, and partly because of the high cost and complexity of doing three-dimensional simulations in this geometry.

Other than the intrinsic three-dimensionality that could develop at high Reynolds numbers, additional three-dimensionality is inherent in the multilouvered geometry near the junction of the louver with the tube surface, along the height of the fin. The angled louver transitions to a flat landing, which extends to the tube surface as shown in Fig. 6. The extent of the transition region is estimated to be $0.5\,L_p^*$ based on structural properties and the manufacturing process used [Halt, 1999]. A consequence of the manufacturing process is that the leading edge of the louver in the transition region instead of being perpendicular to the oncoming flow now exhibits an angle to the flow direction, which is given by $90-\tan^{-1}[1/\{1-\cos\theta\}]$, where $\theta$ is the louver angle. For a 25 degree louver this angle is 5.4 degrees, whereas for a 20 degree louver it reduces to 3.5 degrees. Also during the transition from the louver angle to the flat landing, the open flow area between two subsequent louvers is restricted and creates conditions for strong streamwise velocity acceleration in the region. The three-dimensional geometry could also have a large effect on the onset and spread of spatial instabilities.

Our objective is to study the effect of the three-dimensional louver geometry in the transition zone on the flow and thermal fields generated. The paper describes aspects of the mathematical formulation, the algorithm, spatial discretizations, and the parallel linear solver. Preliminary results are presented.

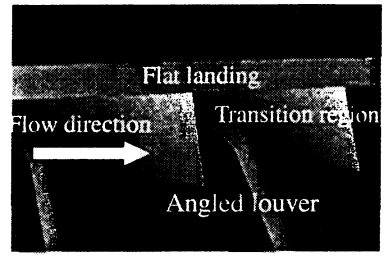


**Fig. 6: Three-dimensional louver geometry near tube junction.**

## NUMERICAL METHODOLOGY

### Mathematical Formulation and Governing Equations

To calculate the flow and thermal fields, we map the Navier-Stokes and energy equations from physical $(\vec{x})$ to logical/computational space $(\vec{\xi})$ by a boundary conforming transformation $\vec{x}=\vec{x}(\vec{\xi})$, where $\vec{x}=(x,y,z)$ and $\vec{\xi}=(\xi,\eta,\zeta)$. Based on the nomenclature of Thompson et al. [1985], the transformed *non-dimensional* time-dependent incompressible Navier-Stokes and the energy equations are written in strong-conservative form as:

Continuity:

$$\frac{\partial}{\partial \xi_j}\left(\sqrt{g}U^j\right)=0 \tag{1}$$

Momentum:

$$\frac{\partial}{\partial t}\left(\sqrt{g}u_i\right)+\frac{\partial}{\partial \xi_j}\left(\sqrt{g}U^j u_i\right)=-\frac{\partial}{\partial \xi_j}\left(\sqrt{g}(\vec{a}^j)_i P\right)+\frac{\partial}{\partial \xi_j}\left(\frac{1}{\mathrm{Re}}\sqrt{g}g^{jk}\frac{\partial u_i}{\partial \xi_k}\right)+\sqrt{g}S_{u_i} \tag{2}$$

Energy:

$$\frac{\partial}{\partial t}\left(\sqrt{g}T\right)+\frac{\partial}{\partial \xi_j}\left(\sqrt{g}U^j T\right)=\frac{\partial}{\partial \xi_j}\left(\frac{1}{\mathrm{Pr}\,\mathrm{Re}}\sqrt{g}g^{jk}\frac{\partial T}{\partial \xi_k}\right)+\sqrt{g}S_T \tag{3}$$

where $\vec{a}^i$ are the contravariant basis vectors[3], $\sqrt{g}$ is the Jacobian of the transformation, $g^{ij}$ is the contravariant metric tensor, $\sqrt{g}U^j=\sqrt{g}\left(\vec{a}_i^j\right)u_i$ is the contravariant flux vector, $u_i$ is the Cartesian velocity vector, $T$ is the temperature, $S_{u_i}$ and $S_T$ are the source terms in the momentum and energy equations, respectively.

[3] The notation $\left(\vec{a}_i^j\right)$ is used to denote the *i-th* component of vector $\vec{a}^j$.

## Formulation for Fully-Developed Flow and Heat Transfer

For computational purposes we approximate the louvered fin geometry by an infinite array of louvers, which results in a simpler system with periodic repetition of the basic unit. The unit computational domain for the base louver geometry is shown in Fig. 7.

Eqns. (1), (2) and (3) are non-dimensionalized by a characteristic length scale, which in this case is taken to be the louver pitch, $L_p^*$, the friction velocity $u_\tau^* = \sqrt{\Delta P_x^* / \rho}$ as the velocity scale, and $q''^* L_p^* / k$ as the temperature scale. Here, $\Delta P_x^*$ is the pressure gradient in the x- direction, $q''^*$ is the specified dimensional constant heat flux on the louver surface, and $k$ is the thermal conductivity of the fluid. The above non-dimensionalization results in a Reynolds number based on friction velocity $\mathrm{Re}_\tau = u_\tau^* L_p^* / \nu$, and Prandtl number $Pr = \nu/\alpha$, where $\nu$ and $\alpha$ are the kinematic viscosity and thermal diffusivity of the fluid, respectively.

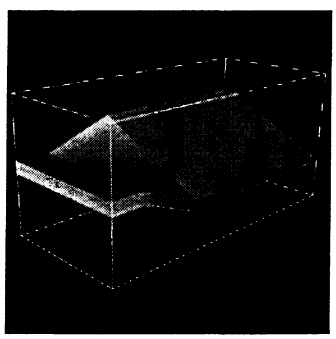

**Fig. 7: Computational domain consisting of one louver representing an infinite array of louvers put together in the streamwise and cross-stream directions.**

The application of periodic boundary conditions in the streamwise direction requires that pressure and temperature be re-formulated as in Patankar et al. [1977]:

$$\begin{aligned} P(x,y,t) &= P_{in} - \beta x + p(x,y,t) \\ T(x,y,t) &= T_{in} + \gamma x + \alpha(x,y,t) \end{aligned} \tag{4}$$

where $P_{in}$ and $T_{in}$ are specified at the inlet of the computational domain, $\beta$=1 and $\gamma = q''\Omega_f / \mathrm{Re}_\tau \, \mathrm{Pr} \, Q_x L_p$[4] are non-dimensional streamwise gradients of pressure and temperature, respectively, $p$ and $\alpha$ are the modified non-dimensional pressure and temperature, $Q_x$ is the calculated mean flow in the x-direction, and $\Omega_f$ is the fin surface area. Hence, eqn. (2) for the $x$-momentum balance can be written in terms of the modified non-dimensional pressure $p$ with an additional source term $S_{u_1} = 1$, which accounts for the mean pressure gradient[5]. Similarly, eqn. (3) for the energy balance can be written in terms of the modified temperature $\alpha$ with an additional source term given by $S_T = -u\gamma$. Periodic boundary conditions can then be applied on $p$ and $\alpha$ in the flow direction. At the louver surface, no slip and no penetration boundary conditions for the velocity, Neumann boundary condition of type

$$\nabla p \cdot \vec{n} = 0 \tag{5}$$

for the modified pressure, and

$$q''_f = -\nabla\alpha \cdot \vec{n} = q'' + \gamma \vec{e}_x \cdot \vec{n} \tag{6}$$

for the modified temperature are applied. In eqns. (5) and (6), $\vec{n}$ is the outward unit vector normal to the louver surface, $\delta\Omega_f$, and $\vec{e}_x$ is the unit vector in the $x$-direction. Further details of the re-formulation can be found in Zhang et al. [1997a].

## Numerical Algorithm

For the time integration of the discretized continuity and momentum equations, we use a projection method [Chorin, 1968; Kim and Moin, 1985]. The temporal advancement is performed in two steps, a predictor step which calculates an intermediate velocity field, and a corrector step which calculates the updated divergence free velocity at the new time step. The predictor step can be fully explicit in time or semi-implicit, in which the viscous terms are treated implicitly. Both methods are incorporated in the present computer program. The semi-implicit method is useful for low Reynolds number flows by allowing larger time steps than what would be allowed by the viscous stability condition. The corrector step, uses the continuity equation to formulate the pressure equation. The computed pressure is then used to update the intermediate velocity field. Symbolically, the two step procedure of the projection method can be written as follows:[6]

Predictor step:

The explicit treatment uses the second-order accurate Adams-Bashforth method, whereas the semi-implicit treatment uses a combination of Adams-Bashforth and Crank-Nicolson methods. First, momentum and energy fluxes across non-matching interfaces are conserved to obtain the conserved quantity $\langle u_i^n \rangle$ or $\langle \alpha^n \rangle$.

Explicit formulation:

$$\frac{\tilde{u}_i - \langle u_i^n \rangle}{\Delta t} = \frac{3}{2} H_i^n - \frac{1}{2} H_i^{n-1}, \tag{7-a}$$

where,

[4] With the non-dimensionalization used, $q''$ and $L_p$ take on a value of unity.

[5] The formulation fixes the mean pressure gradient and lets the flow rate adjust to balance the losses in the calculation domain.

[6] The energy equation is advanced in time by the predictor step.

$$H_i = -\frac{1}{\sqrt{g}}\frac{\partial}{\partial \xi_j}(\langle \sqrt{g}U^j \rangle \langle u_i \rangle) + \frac{1}{\sqrt{g}}\frac{\partial}{\partial \xi_j}\left(\frac{1}{\mathrm{Re}}\sqrt{g}g^{jk}\frac{\partial \langle u_i \rangle}{\partial \xi_k}\right) + S_{u_i} \tag{7-b}$$

Semi-Implicit formulation[7]:

$$\frac{\tilde{u}_i - \langle u_i^n \rangle}{\Delta t} = \frac{3}{2}H_i^n - \frac{1}{2}H_i^{n-1} + \frac{1}{2}\frac{1}{\sqrt{g}}\frac{\partial}{\partial \xi_j}\{\frac{1}{\mathrm{Re}}\sqrt{g}g^{jk}(\frac{\partial \tilde{u}_i}{\partial \xi_k} + \frac{\partial \langle u_i^n \rangle}{\partial \xi_k})\} \tag{8-a}$$

where $H_i = -\frac{1}{\sqrt{g}}\frac{\partial}{\partial \xi_j}(\langle \sqrt{g}U^j \rangle \langle u_i \rangle) + S_{u_i}$ (8-b)

where the superscript ~ denotes the intermediate field, $\langle\ \rangle$, denotes quantities based on conservation of fluxes at non-matching boundaries, $n$, the present time level, and $n+1$, the next time level.

Corrector step:

In this step, we use the continuity equation to derive the pressure equation, which is solved to obtain the pressure field at time level $(n+1)$. The procedure used in formulating the pressure equation is represented as follows:

First the intermediate cell face contravariant fluxes are constructed as follows

$$\sqrt{g}\tilde{U}^j = \sqrt{g}(\vec{a}^j)_i \tilde{u}_i \tag{9}$$

The contravariant flux is then conserved globally at non-matching boundaries to obtain $\langle \sqrt{g}\tilde{U}^j \rangle$. Then, the correction form of the nodal Cartesian velocities and cell face contravariant fluxes are written as:

$$u_i^{n+1} = \tilde{u}_i - \Delta t(\vec{a}^j)_i \left\langle \frac{\partial p^{n+1}}{\partial \xi_j} \right\rangle \tag{10}$$

$$\langle \sqrt{g}(U^i)^{n+1} \rangle = \langle \sqrt{g}\tilde{U}^i \rangle - \Delta t \sqrt{g}g^{ik}\left\langle \frac{\partial p^{n+1}}{\partial \xi_k} \right\rangle \tag{11}$$

Finally, eqn. (11), in conjunction with eqn. (1), is used to derive the pressure equation, which takes the form:

$$\frac{\partial}{\partial \xi_j}\{\sqrt{g}g^{jk}\left\langle \frac{\partial p^{n+1}}{\partial \xi_k} \right\rangle\} = \frac{1}{\Delta t}\frac{\partial \langle \sqrt{g}\tilde{U}^j \rangle}{\partial \xi_j} \tag{12}$$

The pressure field at level $n+1$ is then used to correct the nodal Cartesian velocities and the cell face contravariant fluxes using eqns. (10) and (11), respectively. The use of $\langle\ \rangle$ on the pressure gradient term implies conservation of this quantity at non-matching interface boundaries, during the solution of eqn. (12). Hence, $\sqrt{g}(U^i)^{n+1}$ is automatically conserved when the correction in eqn. (11) is applied to the conserved intermediate field.

[7]In the semi-implicit formulation, at the louver surface we use $\tilde{u}_i = u_i^{n+1} = 0$ in the momentum equations and $\tilde{\alpha} = \alpha^{n+1}$ in the energy equation [Peyret and Taylor, 1985].

## Spatial Discretization

The above governing equations are discretized with a conservative finite-volume formulation. In non-orthogonal coordinate systems, there are a number of choices in the selection of the grid topology and the dependent variable in the momentum equations. In the current work, we adopt a nonstaggered grid topology with Cartesian velocities as dependent variables. The Cartesian velocities, pressure and temperature are calculated and stored at the cell center, whereas contravariant volume fluxes are stored and calculated at the cell faces. For geometric quantities, we calculate and store ($\sqrt{g}a^i$) and the diagonal terms of ($\sqrt{g}g^{ij}$) at the cell faces, and the off-diagonal terms of ($\sqrt{g}g^{ij}$) at the cell centers. Eqn. (7-b) is approximated by second-order central-difference schemes (we drop the $\langle\ \rangle$ notation for convenience).

$$\begin{aligned}\sqrt{g}H_i = &\left(-\sqrt{g}U^1u_i + \frac{1}{\mathrm{Re}}\sqrt{g}g^{1k}\frac{\partial u_i}{\partial \xi_k}\right)_{i+1/2,j,k} \\ &-\left(-\sqrt{g}U^1u_i + \frac{1}{\mathrm{Re}}\sqrt{g}g^{1k}\frac{\partial u_i}{\partial \xi_k}\right)_{i-1/2,j,k} \\ &+\left(-\sqrt{g}U^2u_i + \frac{1}{\mathrm{Re}}\sqrt{g}g^{2k}\frac{\partial u_i}{\partial \xi_k}\right)_{i,j+1/2,k} \\ &-\left(-\sqrt{g}U^2u_i + \frac{1}{\mathrm{Re}}\sqrt{g}g^{2k}\frac{\partial u_i}{\partial \xi_k}\right)_{i,j-1/2,k} \\ &+\left(-\sqrt{g}U^3u_i + \frac{1}{\mathrm{Re}}\sqrt{g}g^{3k}\frac{\partial u_i}{\partial \xi_k}\right)_{i,j,k+1/2} \\ &-\left(-\sqrt{g}U^3u_i + \frac{1}{\mathrm{Re}}\sqrt{g}g^{3k}\frac{\partial u_i}{\partial \xi_k}\right)_{i,j,k-1/2}\end{aligned} \tag{13}$$

where $(i,j,k)$ denote the cell center, and $i\pm1/2, j\pm1/2, k\pm1/2$, the cell faces. Here, particular care is taken to maintain close to second-order accuracy on stretched orthogonal grids. For example, the values of $u_i$ and $\sqrt{g}g^{ij}$ (where $i \neq j$) at cell faces are evaluated through the use of grid based interpolations. For example, the value of $\phi_{i+1/2,j,k}$ at the $\xi$+ cell face is interpolated as

$$\phi_{i+1/2,j,k} = f^m_{i+1/2,j,k}\phi_{i,j,k} + f^p_{i+1/2,j,k}\phi_{i+1/2,j,k} \tag{14}$$

Here, $f^m_{i+1/2,j,k}$ and $f^p_{i+1/2,j,k}$ are interpolation factors based on the arch length ($ds$) along the $\xi$ direction at cells $(i,j,k)$ and $(i+1,j,k)$.

$$f^{m}_{i+1/2,j,k} = ds_{i+1,j,k} / (ds_{i,j,k} + ds_{i+1,j,k}) \tag{15a}$$

$$f^{p}_{i+1/2,j,k} = ds_{i,j,k} / (ds_{i,j,k} + ds_{i+1,j,k}) \tag{15b}$$

For the pressure equation, the source terms are evaluated from a local balance of the intermediate volume fluxes at cell faces surrounding the finite volume, and the coefficient matrix is constructed from the left hand side of eqn. (12), which is similar to the diffusion terms in eqn. (8-a).

$$\begin{aligned}
&\left(\frac{\partial}{\partial \xi_j}\{\sqrt{g}\, g^{jk} \frac{\partial p^{n+1}}{\partial \xi_k}\}\right. \\
&= \left(\sqrt{g}\, g^{1k} \frac{\partial p}{\partial \xi_k}\right)_{i+1/2,j,k} - \left(\sqrt{g}\, g^{1k} \frac{\partial p}{\partial \xi_k}\right)_{i-1/2,j,k} \\
&+ \left(\sqrt{g}\, g^{2k} \frac{\partial p}{\partial \xi_k}\right)_{i,j+1/2,k} - \left(\sqrt{g}\, g^{2k} \frac{\partial p}{\partial \xi_k}\right)_{i,j-1/2,k} \\
&+ \left(\sqrt{g}\, g^{3k} \frac{\partial p}{\partial \xi_k}\right)_{i,j,k+1/2} - \left(\sqrt{g}\, g^{3k} \frac{\partial p}{\partial \xi_k}\right)_{i,j,k-1/2}
\end{aligned} \tag{16}$$

For illustration purposes, we only discretize the first term in eqn. (16):

$$\begin{aligned}
\left(\sqrt{g}\, g^{1k} \frac{\partial p}{\partial \xi_k}\right)_{i+1/2,j,k} &= \left(\sqrt{g}\, g^{11}\right)_{i+1/2,j,k} \left(\frac{\partial p}{\partial \xi}\right)_{i+1/2,j,k} \\
&+ f^{P}_{i+1/2,j,k} \left(\sqrt{g}\, g^{12}\right)_{i+1,j,k} \left(\frac{\partial p}{\partial \eta}\right)_{i+1,j,k} \\
&+ f^{m}_{i+1/2,j,k} \left(\sqrt{g}\, g^{12}\right)_{i,j,k} \left(\frac{\partial p}{\partial \eta}\right)_{i,j,k} \\
&+ f^{P}_{i+1/2,j,k} \left(\sqrt{g}\, g^{13}\right)_{i+1,j,k} \left(\frac{\partial p}{\partial \zeta}\right)_{i+1,j,k} \\
&+ f^{m}_{i+1/2,j,k} \left(\sqrt{g}\, g^{13}\right)_{i,j,k} \left(\frac{\partial p}{\partial \zeta}\right)_{i,j,k}
\end{aligned} \tag{17}$$

Since we store and calculated the diagonal terms of $(\sqrt{g}\, g^{jk})$ at their corresponding cell faces, and the off-diagonal terms at the cell centers, we will only need to discretize the first derivatives of the pressure in the above equation:

$$\left(\frac{\partial p}{\partial \xi}\right)_{i+1/2,j,k} = p_{i+1,j,k} - p_{i,j,k} \tag{18a}$$

$$\begin{aligned}
\left(\frac{\partial p}{\partial \eta}\right)_{i,j,k} &= \left(f^{p}_{i,j+1/2,k}\, p_{i,j+1,k} + f^{m}_{i,j+1/2,k}\, p_{i,j,k}\right) \\
&- \left(f^{p}_{i,j-1/2,k}\, p_{i,j,k} + f^{m}_{i,j-1/2,k}\, p_{i,j-1,k}\right)
\end{aligned} \tag{18b}$$

$$\begin{aligned}
\left(\frac{\partial p}{\partial \eta}\right)_{i+1,j,k} &= \left(f^{p}_{i+1,j+1/2,k}\, p_{i+1,j+1,k} + f^{m}_{i+1,j+1/2,k}\, p_{i+1,j,k}\right) \\
&- \left(f^{p}_{i+1,j-1/2,k}\, p_{i+1,j,k} + f^{m}_{i+1,j-1/2,k}\, p_{i+1,j-1,k}\right)
\end{aligned} \tag{18c}$$

$$\begin{aligned}
\left(\frac{\partial p}{\partial \zeta}\right)_{i,j,k} &= \left(f^{p}_{i,j,k+1/2}\, p_{i,j,k+1} + f^{m}_{i,j,k+1/2}\, p_{i,j,k}\right) \\
&- \left(f^{p}_{i,j,k-1/2}\, p_{i,j,k} + f^{m}_{i,j,k-1/2}\, p_{i,j,k-1}\right)
\end{aligned} \tag{18d}$$

$$\begin{aligned}
\left(\frac{\partial p}{\partial \zeta}\right)_{i+1,j,k} &= \left(f^{p}_{i+1,j,k+1/2}\, p_{i+1,j,k+1} + f^{m}_{i+1,j,k+1/2}\, p_{i+1,j,k}\right) \\
&- \left(f^{p}_{i+1,j,k-1/2}\, p_{i+1,j,k} + f^{m}_{i+1,j,k-1/2}\, p_{i+1,j,k-1}\right)
\end{aligned} \tag{18e}$$

Finally, eqn. (16) can be recast into the following compact form of 19 non-zero coefficients:

$$\left(\frac{\partial}{\partial \xi_j}\{\sqrt{g}\, g^{jk} \frac{\partial p^{n+1}}{\partial \xi_k}\}\right. = A_P p_P + \sum A_{nb} p_{nb} \tag{19}$$

where $A$ denotes the coefficient matrix, the subscript $p$ denotes the main diagonal term, and $nb$ denotes neighboring off-diagonal terms of the pressure coefficient matrix. Typically, for the present calculations the convergence criterion used is *1.e-5* based on the $L_1$ norm of the residual.

## Solution of Pressure Equation

The Laplacian operator in eqn. (19), which is constructed based on grid based interpolations, makes the resulting linear system nonsymmetric on nonorthogonal grids. Further, the presence of nonconformal or non-matching boundaries creates additional strong nonsymmetries. There are many varieties of algorithms for solving large sparse systems of linear equations. These include sparse direct solvers, iterative solvers, including Krylov subspace methods with suitable preconditioners and multigrid methods [Axelsson, 1994]. In our work we use Krylov methods based on the method of Conjugate Gradients (CG) for symmetric systems and BiCGSTAB for nonsymmetric systems. These are coupled with powerful preconditioners based on a two-level Additive Schwarz domain decomposition (DD) method.

By substructuring the original system into smaller systems, the DD method not only reduces the condition number of the original system, but also provided a natural avenue for parallelization. Many different algorithms are used with DD methods [Smith et al., 1996]. Here we use the overlapping boundary method. In a one-level algorithm, the subdomains share information through the interface or the overlapping regions. The convergence rate, however, deteriorates as the number of sub-domains increase. In order to make the algorithms scalable, it is necessary to provide global coupling between distant sub-domains. One common practice is to use a

coarse space, and to solve an appropriate problem on the coarse grid. This approach is called two-level domain decomposition.

For a system of linear equations given by, $Ax = b$, where for simplicity it is assumed that the coefficient matrix $A$ is symmetric positive definite and that the conjugate gradient (CG) method can be applied[8]. If a non-singular matrix $M$ can be made to approximate the matrix $A$ in some way, the preconditioned system $M^{-1}Ax = M^{-1}b$, which has the same solution as the original system, can exhibit much better spectral properties or a lower condition number, resulting in faster convergence.

The Additive Schwarz (AS) preconditioner involves solutions of smaller systems on subdomains in a domain decomposition approach. The domain $\Omega$ is partitioned into $N$ subregions $\{\Omega_i', i = 1,....N\}$ by extending one cell at each subdomain boundary. Let $A_i$ be the coefficient matrix defined on $\Omega_i'$ and let the $n_i \times n$ matrix $R_i$ represent the algebraic restriction of an $n$-vector on $\Omega$ to a $n_i$-vector on $\Omega_i'$, and let its transpose matrix $R_i^T$ represent the extension of an $n_i$-vector to a $n$-vector by padding with zeros. Further, we introduce another mesh on $\Omega$, consisting of $n_0$ cells. This new mesh is coarser than the original mesh, and it is denoted by $\Omega_0'$. We define $A_0$ as the coefficient matrix on $\Omega_0'$, and we further introduce a $n_0 \times n$ matrix $R_0$ to restrict any fine-mesh vector into its corresponding coarse mesh vector (as in a two-level multigrid method). Let $R_0^T$ be the transpose of $R_0$, then $R_0^T$ prolongates a coarse mesh vector to a fine mesh vector. Then the additive Schwarz preconditioner is given by

$$M^{-1} = \sum_{i=0}^{N} M_i^{-1} = \sum_{i=0}^{N} R_i^T A_i^{-1} R_i \tag{20}$$

It has been shown that the convergence rate of the Additive Schwarz PCG (ASPCG) method is independent of the fine-grid size and the coarse-grid size [Dryja and Widlund, 1992]. However, an optimal preconditioner does not necessarily provide the least execution time or computational complexity. For example, the equation above requires exact solutions of subdomain problems and a coarse problem, and in general it is wasteful to solve these sub-problems exactly, particularly when the iterates are still far from the true solution. On the other hand, inexact sub-problem solvers often lead to improved execution time. Hence, we approximate $\tilde{A}_i^{-1}$ at the algebraic level, and the preconditioner is now given by

$$M^{-1} = \sum_{i=0}^{N} R_i^T \tilde{A}_i^{-1} R_i \tag{21}$$

$\tilde{A}_i^{-1}$ is obtained through a polynomial approximation (Dubois et al. 1979). Let $\tilde{A}_i = E_i - F_i$, then

$$\tilde{A}_i^{-1} = \left( \sum_{j=0}^{m-1} \left( E_i^{-1} F_i \right)^j \right) E_i^{-1} \tag{22}$$

where $m$ is the number of iterations of the polynomial preconditioner. In Wang and Tafti (1999), both Richarson or point Jacobi and Symmetric Successive Over-relaxation (SSOR) were evaluated as the inexact domain solves.

Hence, in the ASPCG method, the global system on $\Omega$ is solved by a Krylov method, and the preconditioner uses an Additive Schwarz method. Each sub-domain solve in the preconditioner is independent of the other sub-domains and hence provides a high degree of parallelism. Each time a sub-domain is visited, a number of sweeps or iterations, $m$ are performed on the sub-domain to relax the solution. At this point the residue on $\Omega_i'$ is restricted to the coarse level, $\Omega_0'$, and a similar relaxation is performed on the coarse level. The coarse level size $n_0$ is equal to $N$, the number of sub-domains. After a fixed number of iterations, the correction from the coarse level is prolongated back to $\Omega_i'$. The coarse level in this framework, works much like in multigrid algorithms. The key to the success of the method in realizing good cache performance is that the size $n_i$, of each subdomain should be small enough to fit in cache (usually L2 or secondary cache), and the number of relaxation sweeps $m$ should be as large as possible. Fig. 8-a from Wang and Tafti (1999), shows the optimal (minimum CPU time) performance gain obtained by the AS preconditioning versus global preconditioning for a Richardson or point-Jacobi smoother on a number of cache based architectures. The performance gain was largest on architectures with the greatest disparity in processor speed and memory bandwidth and latency.

The ASPCG method was found to provide the following benefits [Wang and Tafti, 1999]:

- Reduced the number of iterations for convergence in the Krylov solver by a factor of two to three, hence reducing the number of global inner products and matrix-vector products in the Krylov solver.
- Increased performance by a factor of two-three.
- Decreased the overall CPU time by nearly an order of magnitude.

[8] The Additive Schwarz preconditioner is not confined to the CG method but can be used with any other nonsymmetric Krylov solver as well.

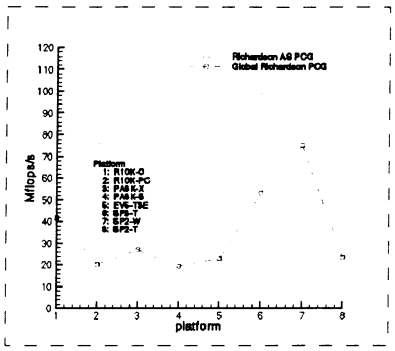


(a)

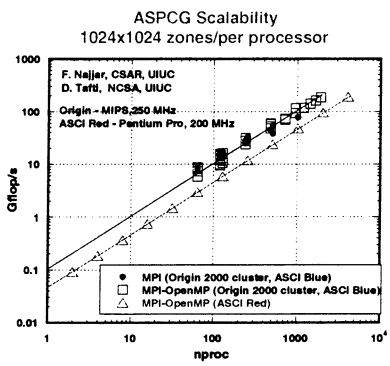


(b)

**Fig. 8: (a) Uniprocessor performance enhancement of ASPCG versus Global PCG on different microprocessor based architectures; (b) Parallel scalability of ASPCG on two ASCI platforms.**

The parallel implementation of the AS method is relatively straightforward. The additive algorithm provides a high degree of parallelism as well as data locality [Wang and Tafti, 1998b]. Fig. 8-b shows scalability studies on the ASCI Blue Origin 2000 cluster at Los Alamos and ASCI Red Intel machine at Sandia for a model problem. The domain size on each processor is maintained at 1024x1024 cells, with 1024 sub-domains of size 32x32 for cache performance. The number of relaxation sweeps on $\Omega_i'$ is 40, and 100 on the coarse level, $\Omega_0'$. The calculations on the ASCI Blue are run across a cluster of Origins using only MPI (in and across Origins) or a combination of MPI-OpenMP. In the hybrid MPI-OpenMP model, MPI processes are not only used across Origins but within Origins as well. For each *nproc* (total number of processors used) in the figure, the multiple data points correspond to different combinations of MPI and OpenMp threads executed across different number of Origins. On the ASCI Red, OpenMp is used within each two processor node. In all cases, ASPCG shows excellent scalability and performance.

## Interpolation at Periodic Boundaries

Periodic boundary conditions are implemented by utilizing ghost cells at the boundary of the calculation domain. Because of the restrictions put by the louvered geometry on the mesh, which has to conform to both the angled louver and the periodic box boundaries, the resulting mesh distribution on boundary planes ($\xi$+ - $\xi$- and $\eta$+ - $\eta$- boundaries) do not match. Hence, each time periodic boundary conditions are applied, the values have to be interpolated from one face to the other. As a result, for each face we construct four bilinear interpolation matrices (one for cell centered variables, and one each for the three cell face fluxes), which map the solution vectors from one face to the other. Since the mesh is stationary, the mapping functions are calculated at the beginning and used throughout the calculation.

## Integral Adjustments at Periodic Boundaries

Integral adjustments are used to account for the errors introduced during interpolations. At the beginning of each time step, momentum and energy fluxes are conserved at periodic boundaries by imposing the equality

$$\sum_{\xi^+ blk} \left\langle \sqrt{g} U^1 \right\rangle \phi = \sum_{\xi^- blk} \left\langle \sqrt{g} U^1 \right\rangle \phi \tag{23}$$

in the $\xi$- direction, where $\phi = u_i$ or $\alpha$ are the interpolated values. The equality is used to obtain the conserved quantity $<\phi>$.

The intermediate volume fluxes in eqn. (9) are first calculated from the interpolated intermediate velocities. The calculated fluxes, however, do not satisfy the integral flux balance across the periodic boundary.

$$\sum_{\xi^+ blk} \sqrt{g} \tilde{U}^1 = \sum_{\xi^- blk} \sqrt{g} \tilde{U}^1 \tag{24}$$

Therefore, a check is performed to identify and correct the integral flux imbalance to obtain $\left\langle \sqrt{g} \tilde{U}^1 \right\rangle$.

Basically, there are two choices to adjust the fluxes. One is to scale them proportionally and the other is to adjust them linearly. Proportional scaling may have difficulties when the mean mass flux across the boundary is close to zero, whereas linear adjustment (where a constant value is added) may smear recirculation zones near the interface. Since the present interpolation scheme is second order accurate, the interpolation error is very small. Therefore, we choose to adjust the volume flux linearly for the sake of robustness. However, for small values of $\sqrt{g} U^1$ in eqn. (23), even a linear adjustment has the potential of leading to instabilities, since to obtain $<\phi>$, the total flux needs to be divided by this quantity.

For the pressure equation, the pressure at the ghost cell is first interpolated from the relevant boundary. This pressure then serves as a boundary condition for the interior values. For each iteration in the pressure equation solver, eqn. (17), or its equivalent, is first evaluated and then integrated over the relevant boundary. Ideally, the integral value of the pressure gradient at the east face should be equal to that at the west face. In reality, however, due to the interpolation error, this property

is usually not preserved. Based on the difference of the two integral values, a constant value is then added/subtracted to the pressure at the ghost cells interior to the boundary in order to guarantee the equality of the two integral values. Such an adjustment automatically guarantees an integral flux balance for the updated volume fluxes in eqn. (11).

## Three-Dimensional Mesh and Parallel Decomposition

Fig. 9 shows the three-dimensional louver geometry and the surface mesh for a louver angle of 25 degrees, fin pitch ratio of 1.0, and louver thickness ratio of 0.1. The angled portion of the louver extends for 1.5 $L_p^*$, the transition zone for 0.5 $L_p^*$, and the flat landing for 0.25 $L_p^*$ to the tube wall. The computational mesh consists of 98 zones each in $\xi$- and $\eta$- directions, and 96 zones in the $z$-direction along the fin height. The grid is clustered in the vicinity of the louver, in the transition zone and wall region. Fig. 9 shows the distribution of $\Delta z$ versus $z$. The mesh is coarsest in the two dimensional region of the geometry and finest at the beginning and end of transition, and near the wall. A linear transition profile is assumed between the angled louver and the flat landing. As the louver transitions to the flat landing, the gap which exists between adjacent louvers (or between the leading and trailing edges of louvers and the calculation domain boundaries), closes completely. In a structured grid framework this results in a "collapsed grid" or a singularity at the location where the transition region meets with the flat landing. In order to avoid the singularity, we maintain a small gap of 0.013 $L_p^*$ at this junction.

The mesh is partitioned into sixteen pieces in the spanwise $z$-direction. Each piece (98x98x6) is assigned to a processor in a distributed programming environment.

## Initial and Boundary Conditions

Periodic boundary conditions are applied in the streamwise and cross-stream direction. Both the $\xi$- and the $\eta$- direction boundaries are non-matching or nonconformal for the angled louver and transition region, and the interpolation and conservation procedures outlined in preceding sections are used. Once the louver transitions to the flat landing, the boundaries are conforming and no interpolations are necessary. It was found that in the region where the louver flattened out, and the flow aligned itself primarily to the streamwise direction, the small values of the cross-stream volume fluxes and velocity at the top and bottom boundaries in the $\eta$- direction produced instabilities during the application of eqn. (23) for the conservation of fluxes. Hence, the conservation of momentum and energy flux at non-matching boundaries is not strictly imposed. However, we note the errors introduced by this are minimal (of order $1\times10^{-4}$ to $1\times10^{-5}$) in the mean quantities.

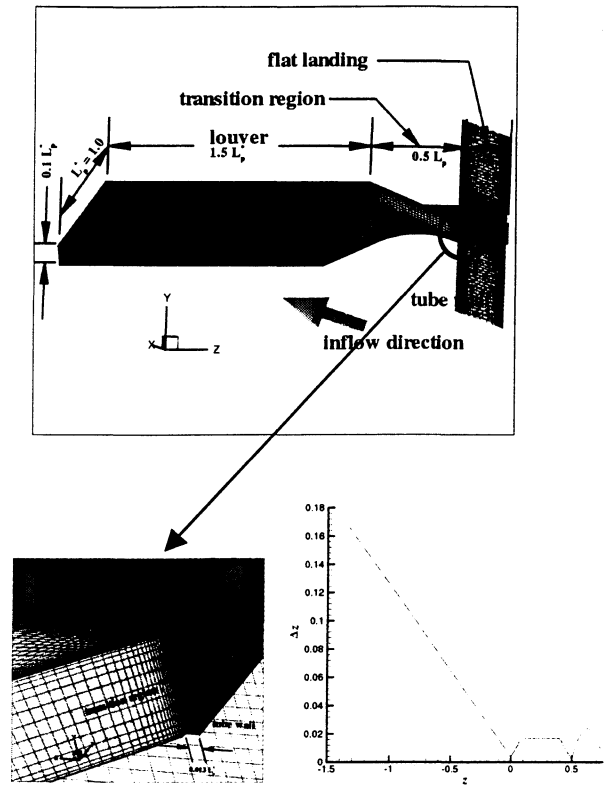


**Fig. 9: Computational geometry and mesh distribution.**

In the spanwise direction, symmetry boundary conditions are applied to the angled louver at $z$ = -1.5, whereas no slip, no penetration wall boundary conditions are applied on the tube surface with a zero heat flux boundary condition. No slip, no penetration, constant heat flux boundary conditions are imposed on the louver. More details about the imposition of boundary conditions on the louver can be found in Tafti et al. [1999].

Initial conditions are obtained from an analogous two-dimensional simulation over the angled louver. The two-dimensional solution is reproduced in the spanwise direction along the height of the fin. Since the flow rate adjusts to the imposed pressure gradient, it is much more economical to run a separate two-dimensional simulation, which gives a fairly good estimate of the bulk flow velocity to begin with, than to simulate the same transient in the three-dimensional calculations.

## Computational Details

The calculations are performed on 16 processors of SGI-Cray Origin 2000. For cache performance in the pressure solver, each processor domain is broken up into virtual blocks of size 8x8x1, on which the Additive Schwarz preconditioner is applied. The coarse level on each processor is of size 12x12x6. The point Jacobi method is used for the inexact solves in each domain and on both the levels. The Reynolds number, $Re_\tau$, is set at 400, which gives a bulk Reynolds number, based on the

calculated bulk velocity and louver pitch, of approximately 1100. The time step used is $1\times10^{-5}$. After the initial transient during the first 10-20,000 time steps, the calculation takes 5.3 *μsecs*/time step/zone of wall clock time. This includes calculating the *mean* and *rms* statistics at each time step.

## RESULTS

Fig. 10 plots the time evolution of the spatially averaged Nusselt number calculated on the louver surface. After the initial transient, the Nusselt number approaches a quasi-stationary state at $t$ = 2.0. Although, the flow may not be fully stationary, and further time integration may be necessary, it is highly unlikely that the essential flow and heat transfer characteristics will change substantially. Hence, for the results presented in this paper, it is assumed that the flow is near stationarity, and the mean quantities presented will be within 5-10 % of their final values. The mean quantities are obtained by averaging for the last two non-dimensional time units (from $t$ = 2-4).

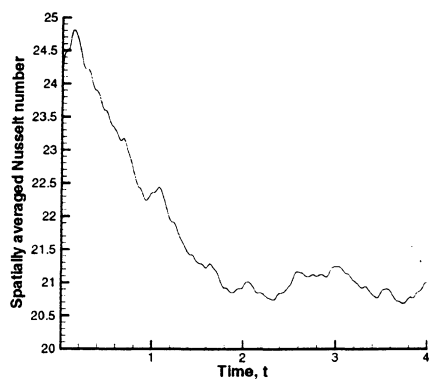


**Fig. 10: Temporal evolution of the spatially averaged Nusselt number.**

### Instantaneous Flow Structures

Two types of identifiable coherent structures can be found in the flowfield. Spanwise vortices generated at the leading edge of the louver are found on the top surface. These develop from leading edge shear layer instabilities. Fig. 11(a-b) shows the plot of instantaneous streamlines in $\zeta$- or $z$- planes at two locations along the fin height. Near the symmetry line at $z$ = -0.97, the flow is mostly two-dimensional in nature. Two vortices are found to exist on the louver surface, one of which has been shed from the shear layer, and the other which is forming. In the middle of the transition zone ($z$ = 0.25), the flow is strongly three-dimensional as evidenced by the streamline patterns and the spanwise vortices are weakened considerably. Only a much smaller, downstream vortex is visible.

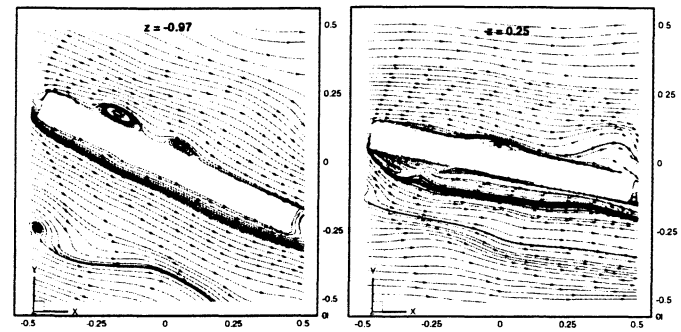


(a) (b)

**Fig. 11: Instantaneous streamlines in two $z$- planes (a) on the angled portion of the louver; (b) and in the middle of the transition zone.**

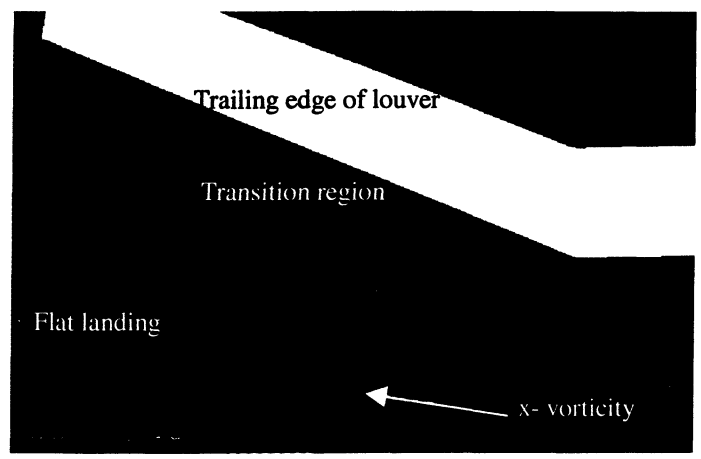


**Fig. 12: Instantaneous streamtubes injection near the leading edge of the louver near the junction with the flat landing.**

In the region where the louver meets the flat landing, strong positive coherent streamwise vorticity is produced in the wake of the louver. The vortex is drawn to the bottom side of the following louver. Although, the core of the vortex is small, it is very energetic. As it passes over the surface of the louver, its interaction with the louver surface produces additional streamwise vorticity of the opposite sign. Fig. 12 shows a snapshot of instantaneous stream tubes injected in the leading edge region of the louver. The streamwise vorticity starts out near the leading edge but diffuses quickly as it travels downstream. It moves across the transition region from $z$ = 0.4 to 0.2, in the direction away from the flat landing. The origin of this structure is studied in more detail in the following section.

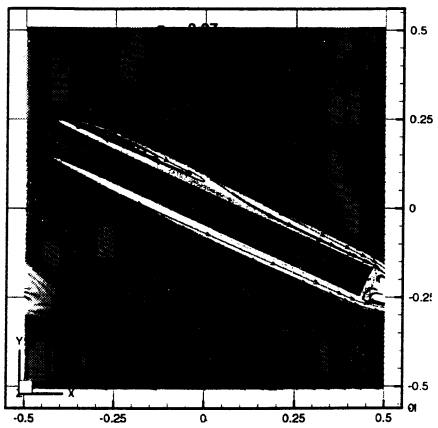


**Fig. 13: Mean planar streamlines superimposed on mean thermal field on a $z$-plane cutting through the angled louver.**

## Time Averaged Flow and Thermal Fields

Fig. 13 plots the mean streamlines superimposed on thermal field at z = -0.97. A recirculation zone exists on the top surface. The thermal boundary layer on the top surface is thicker than that on the bottom surface of the louver. Generally, the effect of the large-scale vortices is to shorten the recirculation region and enhance heat transfer downstream of it. On the bottom surface, because the oncoming flow impinges near the leading edge, the thermal boundary layer is thinnest in this region and increases downstream. The general flow is quite well louver directed at this Reynolds number and thermal wake effects on heat transfer are weak. It is only after the thermal wake is considerably weakened or diluted that it impinges on the top leading edge of the louver.

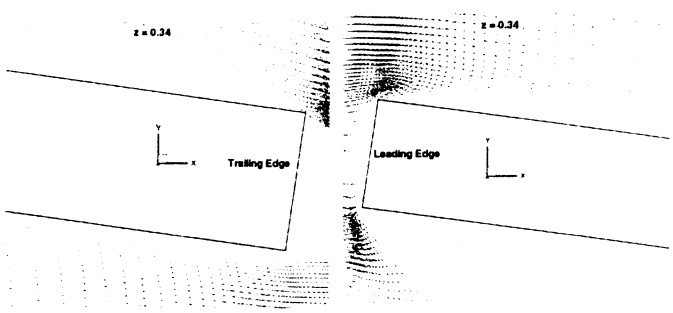


(a) (b)

**Fig. 14: Magnified view of velocity vectors at the trailing and leading edge of the louver in the transition region at $z$ = 0.34.**

As the louver transitions to the flat landing, the effective flow area available between two louvers progressively decreases. Also, the trailing and leading edges of the louver, gradually align themselves in the same horizontal plane. Fig. 14 shows the velocity vectors in a $z$- plane at $z$ = 0.34 at the trailing and leading edge of the louver. Because of the restricted flow area, there is strong flow acceleration at the trailing edge of the louver. The accelerating flow coming off the trailing edge directly impinges on the leading edge near the top of the louver. Part of the stream accelerates to the top louver surface and part of it is drawn underneath. The part which accelerates to the top is much closer to the louver surface, than the part at the bottom which is far from the louver. The part which accelerates to the bottom of the louver, picks up streamwise vorticity and manifests itself as a jet of concentrated vorticity, which is shown instantaneously in Fig. 12. As a consequence of the strong acceleration and distance from the bottom surface, a streamwise recirculation zone forms on the bottom surface, which exists from $z$ = 0.21 to $z$ = 0.45. Fig. 15 at $z$ = 0.28, shows the magnitude of streamwise velocity. The blue region on the lower surface is the recirculation zone. The high velocity stream which is drawn downward is sandwiched between the negative low velocity wake from the trailing edge. There is also evidence of strong velocity acceleration on the top surface of the louver near the trailing edge.

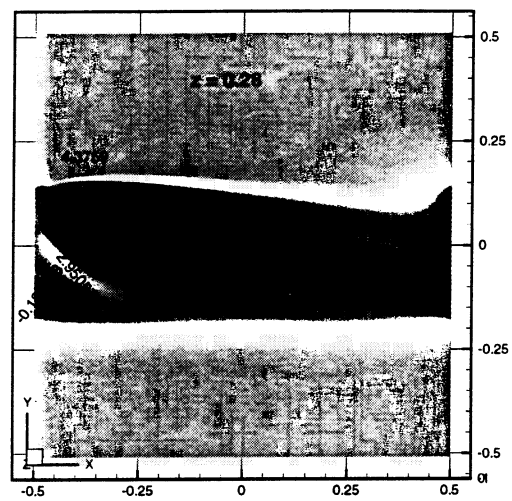


**Fig. 15: Magnitude of streamwise velocity at $z$ = 0.28 in the transition region.**

Fig. 16(a-d) shows thermal fields at $z$ = 0.21, 0.28, 0.375, and 0.435 in the transition region. One of the consequences of the louver flattening out is the thermal wake from the louver starts interfering with the bottom surface of the louver immediately downstream of it. Hence in this region, the combination of the thermal wake effect and the streamwise recirculation reduce the heat transfer coefficient on the lower surface of the louver. On the other hand, the accelerating velocity field on the top surface and its close proximity to the louver surface increases the heat transfer coefficient. This can be surmised by the relatively thin thermal boundary layer on the top surface.

Fig. 17(a-d) plots the streamwise vorticity calculated from the time averaged flowfield at different $x$- planes. The first plane at $x$ = -0.5 lies upstream of the leading edge of the louver or downstream of the trailing edge of the preceding louver. Strong coherent streamwise vorticity centered about $z$ = 0.38 and $y$ = -0.05 is found in this plane. This vorticity first appears in the wake of the preceding louver at $x$ = 0.486. As the vortex jet moves along the bottom surface of the louver, its interaction

with the louver surface produces another coherent structure of the opposite sign. This is visualized at $x$ = -0.3 which is downstream of the louver leading edge. The structure with negative $x$- vorticity is much larger than the original jet but weaker and more diffuse. It extends from $z$ = 0.24 to 0.44 and is centered around $y$ = -0.08. By this time the original jet has diffused considerably. At $x$ = 0.1, which is near the center of the louver, the secondary vorticity is still present, whereas there is no sign of the original jet[9]. By $x$ = 0.3 the secondary vortex has weakened considerably and its center has moved to $z$ = 0.29. Fig. 18 plots the three-dimensional streamlines which capture the vorticity at the bottom of the louver. The seeds are injected at $x$ = -0.47, between $z$ = 0.29 and 0.51, just below and downstream of the leading edge of the louver.

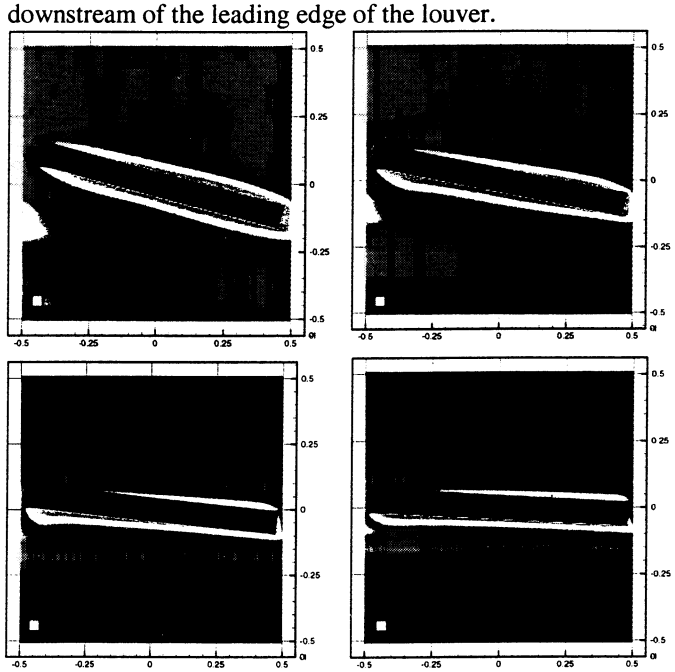

**Fig. 16: Mean thermal fields at $z$ = 0.21, 0.28, 0.375, and 0.435 in the transition region. As the louver flattens out, the thermal wake of the preceding louver interferes with the bottom surface.**

In Fig. 19 the mean temperature contours are plotted in $x$-planes, $x$ = -0.3, 0.1, and 0.3, which coincide with those in Fig. 17. In all cases the thermal boundary layer is thinner, signifying heat transfer augmentation, in the region where the secondary vorticity impinges (upstream of the vortex core) or brings in fluid to the louver surface. We also find evidence of thermal wake interference from the previous louver in this region at $x$ = -0.3. However, by $x$ = 0.1, the thermal wake is considerably attenuated.

Fig. 20 plots the time mean Nusselt number on the top and bottom surface of the louver in the transition region and the flat landing. On the bottom surface, two main patterns are evident. One of them follows the same trajectory as the jet in Fig. 18. In this pattern, the Nusselt numbers are low in the leading edge central core region, and gradually increase in the downstream direction, and as one moves outward from the core. The low Nusselt numbers are a consequence of the streamwise recirculation zone which forms at the bottom of the louver near the leading edge and also the effect of the thermal wake from the previous louver. The other pattern of higher Nusselt numbers is positioned between the jet and the flat landing. Over here the Nusselt numbers are higher and increase as we move downstream along the louver surface. This is a consequence of the secondary vorticity generated by the vortex jet and its motion which brings in free-stream fluid near the louver surface.

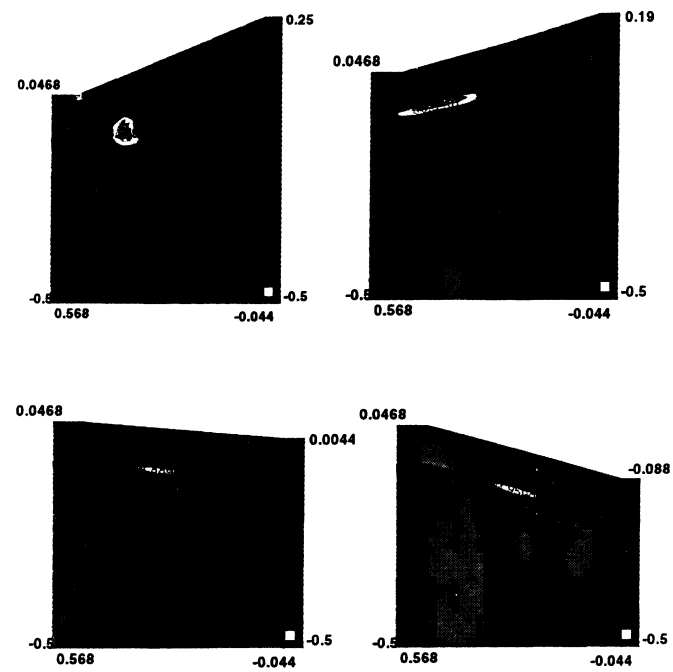


**Fig. 17. Contours of mean $x$-vorticity at $x$- planes starting upstream of the leading edge of the louver and moving downstream. Only the region below the louver in the transition region is shown.**

On the top surface, the Nusselt numbers are about an order of magnitude higher in the leading edge region and gradually decrease in the downstream direction. As the trailing edge is approached it increases again. Both these effects are attributed to the high fluid velocities in the proximity of the louver surface and their effect on the heat transfer coefficient.

[9] Flow animations show that the jet is quite unsteady in the downstream half so even though it may be present instantaneously, the time averaged flow may not be able to reproduce it.

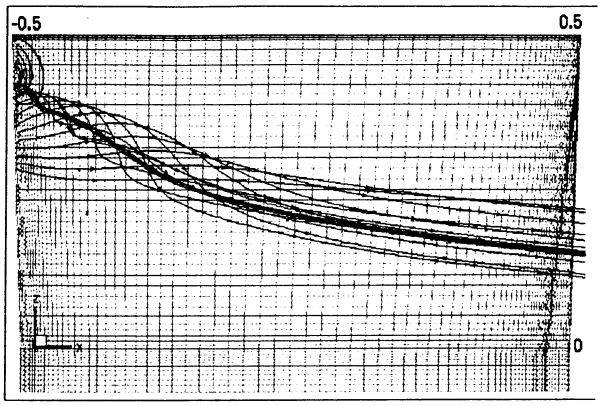


**Fig. 18. Three-dimensional mean streamlines identifying the rotational vorticity imparted to the mean flow in the leading edge region of the louver. The seeds are injected below, near the leading edge of the louver and the view shows the bottom of the louver.**

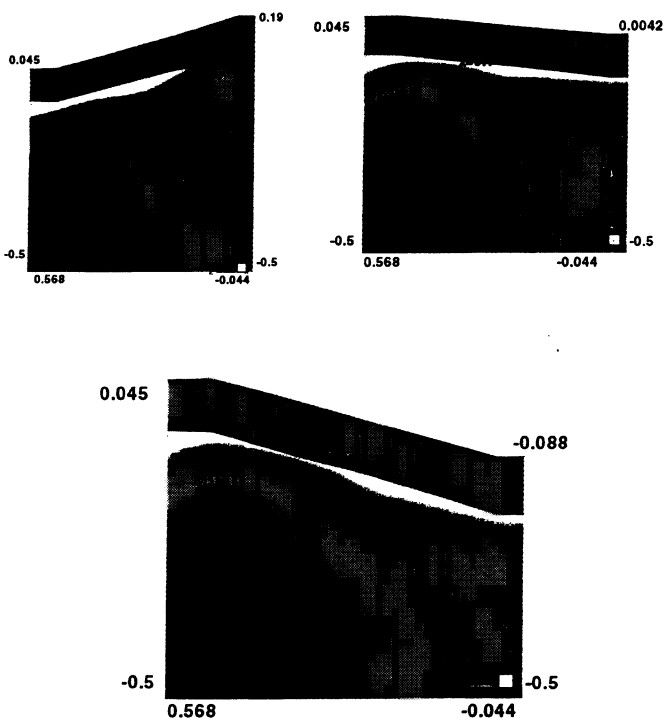


**Fig. 19: Contours of the mean thermal field at $x$-planes along the bottom surface of the louver in the transition region. There is a strong correlation between regions of high heat transfer (thin thermal boundary layers) and the location of coherent $x$-vorticity in Fig. 17.**

Finally, Fig. 21 plots the variation of Nusselt number across the fin height, which is presented as piecewise averages. In the angled part of the louver, the Nusselt number is higher on the bottom surface because of the absense of any recirculation and the fact that the flow impinges near the leading edge on the bottom side. As we move into the transition region, there is a sharp drop in the Nusselt number on the bottom surface at the beginning of transition, with a slight recovery towards the end. On the other hand, the Nusselt number on the top surface increases sharply and reaches a maximum at $z$ = 0.4. The average Nusselt number is highest in the transition region and lowest on the flat landing.

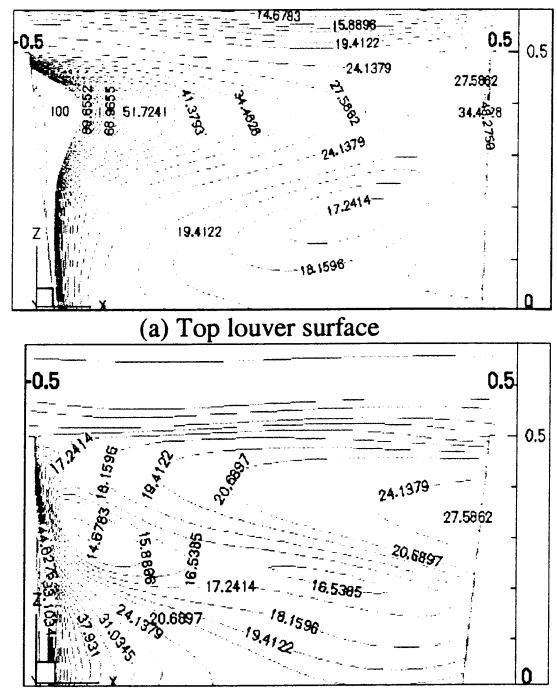


(a) Top louver surface

(b) Bottom Louver surface

**Fig. 20: Mean Nusselt number distribution in the transition region on top and bottom surface of louver.**

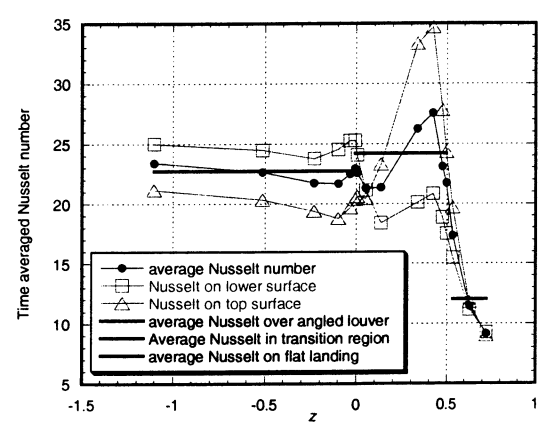


**Fig. 21: Piecewise averaged mean Nusselt number distribution along fin height.**

## SUMMARY AND CONCLUSIONS

Large-eddy simulations of flow and heat transfer are performed in a complex multilouvered fin. The numerical algorithm, discretization procedures, the treatment of flow variables at non-matching interfaces, and the parallel computing technology are described. A single periodic angled louver, its transition to a flat landing, and the tube surface are simulated. The complex domain is resolved by 1 million zones and the calculations are performed in parallel on 16 processors of the SGI-Cray Origin 2000.

Preliminary results are given for a louver angle of 25 degrees, fin pitch and thickness ratio of 1.0 and 0.1, respectively, and a Reynolds number of 1100, based on the bulk flow velocity and louver pitch. The flow in the transition region is strongly three-dimensional and unsteady. A number of new flow features are identified in the transition region which have a large effect on the heat transfer coefficient. Chief among them is the generation of a vortex jet in the region where two louvers come together with the flat landing.

Future work will focus on gaining a deeper understanding of this flow. The effects of geometry variations and Reynolds number will be investigated to quantify the effect on heat transfer, not only on the louver, but also on the tube surface.

## ACKNOWLEDGMENTS

Dr. X. Zhang was supported by the Air Conditioning and Refrigeration Center, Department of Mechanical and Industrial Engineering, University of Illinois, Urbana Champaign. Supercomputing time was granted by the NSF PACI program through the national resource allocation committee.

## REFERENCES

Achaichia, A. and Cowell, T. A., 1988a, Heat Transfer and Pressure Drop Characteristics of Flat tube and Louvered Plate Fin Surfaces, *Experimental Thermal and Fluid Science*, Vol. 1, pp. 147-157.

Achaichia, A. and Cowell, T. A., 1988b, A Finite Difference Analysis of Fully Developed Periodic Laminar Flow in Inclined Louvered Arrays, Proceedings of *2nd UK National Heat Transfer Conference*, Glasgow, Vol. 2, pp. 883-888.

Achaichia, A., Heikal, M. R., Sulaiman, Y. and Cowell, T. A., 1994, Numerical Investigation of Flow and Friction in Louver Fin Arrays. *10th Int. Heat Transfer Conf., Heat Transfer 1994*, Vol. 4, pp. 333-338.

Akselvoll K. and Moin, P., 1995, Large Eddy Simulation of Turbulent Confined Coannular jets and Turbulent Flow over a Backward Facing Step, *Report TF-63*, Thermosciences Div., Dept. mech. Eng., Stanford University, Stanford, CA 94305.

Anderson, K., Gropp, W., Kaushik, D, Keyes, D. and Smith B., 1999, Achieving High sustained Performance in an Unstructured Mesh CFD Application, Bell Prize Award paper, *Proceedings SC'99*.

Axelsson, O., 1994, Iterative Solution Methods. Cambridge University Press.

Baldwin, S.J., White, P.R.S., Al-Daini, A. J. and Davenport, C.J., 1987, Investigation of the Gas Side Flow Field in Multilouver Ducts with Flow Reversal, *5th Int. Conf. on Numerical Methods in Laminar and Turbulent Flow*, Montreal, Vol. 5, Pt. 1, pp. 482-495.

Bardina, J., Ferziger, J. H. and Reynolds, W. C., 1983, Improved turbulence models based on large eddy simulation of homogeneous incompressible turbulence, Stanford University, report TF-19.

Beaudan, P. and Moin, P., 1994, Numerical Experiments on the Flow Past a Circular Cylinder at Sub-Critical Reynolds Number, *Rep. No. TF-62,* Thermosciences Division, Department of Mechanical Engineering, Stanford University.

Beauvais, F. N., 1965, An Aerodynamic Look at Automobile Radiators, *SAE* Paper No. 65070.

Boris, J. P. and Book, D. L., 1973, Flux-Corrected Transport. 1. SHASTA, A Fluid Transport Algorithm That Works, *J. Comput. Phys.* Vol. 11, No. 1, pp. 38-69.

Boris, J.P., Grinstein, F.F., Oran, E.S. and Kolbe, R.L., 1992, New Insights into large eddy simulation, *Fluid Dynamics Research*, vol. 10, pp. 199-228.

Cai, X.-C., Gropp, W. D., Keyes, D. E., Melvin, R. G. and Young, D. P., 1996, Parallel Newton-Krylov-Schwarz algorithms for the transonic full potential equation. *NASA CR-198341, ICASE report No. 96-39*, Institute for Computer Applications in Science and Engineering.

Chang, Y. and Wang, C., 1997, A Generalized Heat Transfer Correlation for Louver Fin Geometry. *Int. J. Heat Mass Transfer*, Vol. 40, No. 3, pp. 533-544.

Chorin, A. J., 1968, Numerical Solution of the Navier-Stokes Equations, *Maths. Comput.*, vol. 22, pp. 745-762.

Davenport, C. J., 1983, Heat Transfer and Flow Friction Characteristics of Louvered Heat Exchanger surfaces, Heat Exchangers: Theory and Practice, Taborek, J., Hewitt, G. F. and Afgan, N. (eds.), pp. 397-412, Hemisphere, Washington, D. C.

DeJong, N. C., and Jacobi, A. M., 1999, Flow, Heat Transfer and Pressure Drop Interactions in Louvered-Fin Arrays, ACRC TR-146.

Domaradzki, J. A. and Saiki, E. M., 1997, A subgrid-scale model based on the estimation of unresolved scales of turbulence, *Phys. Fluids* 9 (7), 2148.

Domaradzki, J. A. and Loh K.-H., 1999, The subgrid-scale estimation model in the physical space representation, *Phys. Fluids*, 11(8), 2330.

Dryja, M. and Widlund, O.B., 1992, Additive Schwarz methods for elliptic finite element problems in three dimensions. In *Fifth conference on domain decomposition methods for partial differential equations*. SIAM, Philedelphia.

Dubois, D., Greenbaum, A. and Rodrigue, G., 1979, Approximating the inverse of a matrix for use in iterative

algorithms on vector processors. Computing, vol. 22, pp. 257.

Ferziger , J. H., 1996, Large Eddy Simulation, Simulation and Modelling of Turbulent Flows – Part III, eds. Gatski, T. B., Hussaini, M. Y. & Lumley, J. L., ICASE/LaRC Series in Computational Science and Engineering, Oxford University Press.

Germano, M., Piomelli, U., Moin, P., and Cabot, W.H., 1991, A dynamic subgrid-scale eddy viscosity model, *Physics of Fluids A*, vol. 3, pp. 1760-1765.

Geurts, B. J., 1997, Inverse modeling for large-eddy simulation, *Phys. Fluids* 9 (12), 3585.

Ghosal, S., Lund, T. S., and Moin, P., 1995, A Dynamic Localization Model for Large-Eddy Simulation of Turbulent Flows, *J. Fluid Mech.*, Vol. 286, 229-255.

Gropp, W., Lusk, E. and Skjellum, A. (1994) Using MPI: Portable Parallel Programming with the Message-Passing Interface. MIT Press.

Halt, D. W., Allan, V. J. and Fish, G. R., 1996, CFD Applications of Automotive Heat Exchangers, FED- 242, *Proceedings of the ASME Fluid Engineering Division*, ASME, pp. 175-180.

Halt, D., 1999, personal communication, Visteon Automotive Systems.

Harlow, F. H. and Welch, J. E., 1965, Numerical Calculation of Time-Dependent Viscous Incompressible Flow of Fluid with Free Surface, *Phys. Fluids*, vol. 8, no. 12, pp. 2182-2189.

Harten, A., 1984, High Resolution schemes for hyperbolic conservation laws, *J. Comput. Phys.*, 49, pp. 357-393.

Hiramatsu, M., Ishimaru, T. and Matsuzaki, K., 1990, Research on Fins for Air Conditioning Heat Exchangers, *JSME International Journal*, Vol. 33, pp. 749-756.

Jordan, S. A. and Ragab, S. A., 1993, On the unsteady and turbulent characteristics of the three-dimensional shear-driven cavity flow, Engineering Applications of Large Eddy Simulations, 1993 ASME Fluids Engineering Summer Meeting, FED 162, 127.

KAI, 1997, Guide Reference Manual. Kuck & Associates, Inc. document number 9607001.

Kim, J. and P. Moin, P., 1985, Application of a Fractional-Step Method to Incompressible Navier-Stokes, *J. Comput. Phys.*, vol. 59, pp. 308-323.

Leonard, B.P., 1991, The ULTIMATE conservative difference scheme applied to unsteady one-dimensional advection, *Comp. Methods in App. Mech, and Engineering* 88, pp. 17-74.

Lesieur, M. and Metais, O., 1996, New Trends in Large-Eddy Simulations of Turbulence, *Ann. Rev. Fluid Mech.* 28, pp. 45-82.

Liu, S., Meneveau, C. and Katz, J., 1994, On the properties of similarity subgrid-scale models as deduced from measurements in a turbulent jet, *J. Fluid Mech.* 275, 83.

Mittal, R. and Moin, P., 1997, Suitability of Upwind-Biased Finite Difference Schemes for Large-Eddy Simulation of Turbulent Flows, *AIAA J.* vol. 35, no. 8, pp. 1415-1417.

MPI2, 1997, MPI-2: Extensions to the Message-Passing Interface. Message Passing Interface Forum. http://www.mpi-forum.org/docs/mpi-20.ps.

Najjar, F. M. and Tafti, D. K., 1996a, Study of Discrete Test Filters and Finite Difference Approximations for the Dynamic Subgrid-Scale Stress Model, *Phys. Fluids*, vol. 8, pp. 1076-1088.

Najjar, F.M. and Tafti, D.K., 1996b, Evaluation of the Dynamic Subgrid-Scale Stress Model in Finite-Difference LES: Effects of Grid Resolution and Inhomogeneous Test Filtering, *FED-Vol. 242*, pp. 229-236, ASME-IMEC, Atlanta, GA.

O'Neil, J. and Meneveau, C., 1997, Subgrid-scale stresses and their modeling in a turbulent plance wake, *J. Fluid Mech.* 349, 253.

Patankar, S. V., C. H. Liu, C. H. and E. M. Sparrow, E. M., 1977, Fully Developed Flow and Heat Transfer in Ducts Having Streamwise-Periodic Variations of Cross-Sectional Area, *Journal of Heat Transfer*, Vol. 99, pp. 180-186, 1977.

Peyret, R. and Taylor, T. D., 1985, Computational Methods for Fluid Flow, Springer-Verlag, New York.

Piomelli, U, Cabot, W., Moin, P. and Lee, S., 1991, Subgrid-scale backscatter in turbulent and transitional flows, *Phys. Fluids A* 3, 1766 .

Piomelli, U., 1993, High Reynolds number calculations using the dynamic subgrid-scale stress model, *Phys. Fluids A* 5, 1484-1490.

Piomelli, U. and Liu, J., 1995, Large-eddy simulation of rotating channel flows using a localized dynamic model, *Phys. Fluids A* 7, 839.

Smagorinksy, J., 1963, General Circulation Experiments with the Primitive Equations. I. The Basic Experiment, *Monthly Weather Review*, vol. 91, pp. 99-164.

Smith, B., Bjørstad, P. and Gropp, W., 1996, Domain Decomposition – Parallel Multilevel Methods for Elliptic Partial Differential Equations. Cambridge University Press.

Springer, M. and Thole, K. A., 1998, Experimental Design for Flowfield Studies of Louvered Fins, *Experimental Thermal and Fluid Science* 18, pp. 258-269.

Suga, K., Aoki, H. and Shingawa, T., 1989, Numerical Analysis on Two-Dimensional Flow and Heat Transfer of Louvered Fins Using Overlaid Grids, *JSM International Journal*, Vol. 33, pp. 122-127.

Suga, K. and Aoki, H., 1991, Numerical Study on Heat Transfer and Pressure Drop in Multilouvered Fins, *ASME/JSME Thermal Engineering Proceedings*, Vol. 4, pp. 361-368.

Tafti, D. K., 1993, Vorticity and Scalar Transport in Separated and Reattached Flow on a Blunt Plate, *Phys. Fluids A* 5(7), pp. 1661-1673.

Tafti D. K., Wang, G., 1998, Application of Embedded Parallelism to Large Scale Computations of Complex

Industrial Flows. *Proceedings of the ASME Fluids Engineering Division*, FED Vol. 247, pp. 123-130.

Tafti D. K., Zhang L.W., and Wang, G., 1999, A Time-Dependent Calculation Procedure for Fully Developed and Developing Flow and Heat Transfer in Louvered Fin Geometries. *Num. Heat Transfer* A, 35(3), pp.225-249.

Tafti D.K., Wang G. and Lin W., 2000, Flow Transition in a Multilouvered Fin Array. *Int. J. Heat Mass Transfer*, vol. 43, No. 6, pp. 901-919.

Thompson, J. F., Warsi, Z. U. A. and Mastin, C. W., Numerical Grid Generation, Foundations and Applications, Elsevier Science Publishing Co., Inc., New York, New York 10017, 1985.

Thuburn, J., 1996, Multidimensional Flux-Limited Advection Schemes, *J. Comput. Phys.*, vol. 123, pp. 74-83.

Top500,1999, http://www.netlib.org/benchmark/top500/top500.list.html.

Wang G., Tafti D.K., 1998a, Uniprocessor performance enhancement by Additive Schwarz preconditioners on Origin 2000. *Advances in Engineering Software*, vol. 29, no. 3-6, pp. 425.

Wang G., Tafti D.K., 1998b, Parallel performance of Additive Schwarz preconditioners on Origin 2000. *Advances in Engineering Software*, vol. 29, no. 3-6, pp. 433.

Wang, G. and Tafti D.K., 1999, Performance Enhancement on Microprocessors with Hierarchical Memory Systems for Solving Large Sparse Linear Systems. *The International Journal of Supercomputing Applications and High Performance Computing*, vol. 13, no. 1, pp. 63.

Webb, R. L. and Trauger, P., 1991, Flow Structure in the Louvered Fin Heat Exchanger Geometry, *Experimental Thermal and Fluid Science*, Vol. 4, pp. 205-217.

Zang, Y. Street, R.L., and Koseff, J.R., 1993, A Dynamic Mixed Subgrid-Scale Model and its Application to Turbulent Recirculating Flows, *Phys. Fluids A*, Vol. 5, 3186-3196.

Zhang, L., Tafti, D. K., Najjar, F., and Balachandar, S., 1997a, Computations of Flow and Heat Transfer in Parallel-Plate Fin Heat Exchangers on the CM-5; Effects of Flow Unsteadiness and Three-Dimensionality. *Int. J. of Heat Mass Transfer*, vol. 40, No. 6, pp. 1325-1341.

Zhang, L., Balachandar, S., Tafti, D. K. and Najjar, F., 1997b, Heat Transfer Enhancement Mechanisms in In-Line and Staggered Parallel Plate Fin Heat Exchangers. *Int. J. of Heat Mass Transfer*, vol. 40, No. 10, pp. 2307-2325.

Zhang, L, Balachandar, S. and Tafti, D. K., 1997c, Effects of Intrinsic Three Dimensionality on Heat Transfer and Friction Loss in a Periodic Array of Parallel Plates. *Numerical Heat Transfer, Part A*, 31, pp. 327-353.

Zhang, H. and Lang, X., 1989, The Experimental Investigation of Oblique Angles and Interrupted Plate Lengths for Louvered Fins in Compact Heat Exchangers, *Experimental Thermal and Fluid Science*, Vol. 2, pp. 100-106.